



RESEARCH ARTICLE

10.1029/2017JF004425

Shortwave Sand Transport in the Shallow Surf Zone

J. A. Brinkkemper^{1,2} , T. Aagaard³ , A. T. M. de Bakker⁴ , and B. G. Ruessink¹

Key Points:

- The shortwave sand flux is the dominating sand flux component under low-energetic conditions with beach accretion
- The magnitude of onshore-directed shortwave sand fluxes scales with velocity asymmetry rather than velocity skewness in the shallow surf zone
- Strong offshore-directed mean currents reduce the shortwave sand flux

Correspondence to:

J. A. Brinkkemper,
joost.brinkkemper@waterproofbv.nl

Citation:

Brinkkemper, J. A., Aagaard, T., de Bakker, A. T. M., & Ruessink, B. G. (2018). Shortwave sand transport in the shallow surf zone. *Journal of Geophysical Research: Earth Surface*, 123, 1145–1159. <https://doi.org/10.1029/2017JF004425>

Received 7 JUL 2017

Accepted 6 APR 2018

Accepted article online 20 APR 2018

Published online 28 MAY 2018

¹Department of Physical Geography, Faculty of Geosciences, Utrecht University, Utrecht, Netherlands, ²Now at Waterproof Marine Consultancy and Services, Lelystad, Netherlands, ³Institute of Geoscience and Natural Resources, University of Copenhagen, Copenhagen K, Denmark, ⁴UMR 7266 LIENSs, CNRS Université de la Rochelle, La Rochelle, France

Abstract Empirical parameterizations of the shortwave sand transport that are used in practical engineering models lack the representation of certain processes to accurately predict morphodynamics in shallow water. Therefore, measurements of near-bed velocity and suspended sand concentration, collected during two field campaigns (at the Sand Engine and Ameland, the Netherlands) and one field-scale laboratory experiment (BARDEXII), were here analyzed to study the magnitude and direction of the shortwave sand flux in the shallow surf zone. Shortwave sand fluxes dominated the total sand flux during low-energetic accretive conditions, while the mean cross-shore current (undertow) dominated the total flux during high-energetic erosive conditions. Under low-energetic conditions, the onshore-directed shortwave sand flux scales with the root-mean-square orbital velocity u_{rms} and velocity asymmetry A_u but not with the velocity skewness. Under more energetic conditions the shortwave flux reduces with an increase in the cross-shore mean current \bar{u} and can even become offshore directed. For all data combined, the contribution of the shortwave flux to the total flux scales with $(-A_u u_{rms})/|\bar{u}|$, with a high contribution of the shortwave flux ($\sim 70\%$) when this ratio is high (~ 10) and low contributions ($\sim 0\%$) when this ratio is low (~ 1). We argue that the velocity asymmetry is a good proxy for the net effect of several transport mechanisms in the shallow surf zone, including breaking-induced turbulence. These field and laboratory measurements under irregular waves thus support the hypothesis that the inclusion of velocity asymmetry in transport formulations would improve the performance of morphodynamic models in shallow water.

1. Introduction

In the surf zone, shortwaves (wave period of 1–20 s) become asymmetric about the vertical axis, with a steep front face and a gentle rear face (i.e., pitched forward), and reduce in height due to energy dissipation through breaking. Both wave asymmetry and breaking-induced turbulence can affect the magnitude and direction of the shortwave sand transport (e.g., Scott et al., 2009; van der A et al., 2009) and therefore prohibit the application of transport formulas designed for deeper water and shoaling wave conditions. The shortwave-driven sand transport is particularly important during low-energetic conditions, when other transport components, that is, long-wave (wave period of 20–200 s) driven transport and transport by mean cross-shore currents, are small (e.g., Aagaard et al., 2013; Osborne & Greenwood, 1992). During these low-energetic conditions, the shortwave sand transport is often crucial for the onshore migration of nearshore bars (e.g., Aagaard et al., 2002; Hoefel & Elgar, 2003) and thus for the recovery of beaches between storms.

The wave orbital velocities in shallow water change analogously with the wave shape and also become skewed in the shoaling zone and asymmetric in the surf zone. While velocity skewed flows were shown to transport sand in the onshore direction (e.g., O'Donoghue & Wright, 2004; Ribberink & Al-Salem, 1994) under flat bed conditions, asymmetric flow was long believed to not induce sand transport (Roelvink & Stive, 1989). However, flow tunnel experiments later showed asymmetric flow to drive sand transport in the direction of the highest acceleration (King, 1991; Ruessink et al., 2011; Silva et al., 2011; van der A et al., 2009; Watanabe & Sato, 2004), which would also be in the onshore direction on a natural beach. This onshore transport has been ascribed to several mechanisms. First, the boundary layer has less time to grow during the large acceleration between maximum negative and maximum positive velocities in comparison with the long duration and small acceleration from maximum positive to negative flow. The vertical gradient in flow velocity is thus larger, and shear stresses are higher during the positive flow phase (Henderson et al., 2004; Nielsen, 1992; van der A et al., 2008). Second, sand stirred during maximum negative flow has less time to settle before

©2018. The Authors.

This is an open access article under the terms of the Creative Commons Attribution-NonCommercial-NoDerivs License, which permits use and distribution in any medium, provided the original work is properly cited, the use is non-commercial and no modifications or adaptations are made.

flow reverses in comparison with sand stirred during the maximum positive flow. This effect is largely dependent on the sediment fall velocity, and a modeling study by Ruessink et al. (2009) indicated that these phase lag effects are only important for fine-medium sands ($\lesssim 250 \mu\text{m}$). Another process that can contribute to the onshore-directed transport is plug flow (Calantoni & Puleo, 2006; Foster et al., 2006; Sleath, 1999), a term to describe an instant mobilization of several centimeters of sand by the horizontal pressure gradient during the strong flow acceleration at the front of the waves. This mobilized sand is then available for transport during the onshore flow phase. The relative contribution of these mechanisms to the onshore transport by velocity asymmetric waves and the variability of these contributions as a function of wave conditions and beach characteristics are, however, unknown.

Strong opposing currents were also found to affect the transport of sand by oscillatory flow, as these currents increase shear stress during the negative-directed flow phase and decrease the shear stress during the positive-directed phase. This effect can reverse the net transport direction, depending on the magnitude of the current and the degree of asymmetry of the oscillatory flow (Ruessink et al., 2011; Silva et al., 2011). In the field, a strong undertow was suggested to enhance shear stress during the offshore-directed flow phase of long waves (de Bakker et al., 2016), and Aagaard et al. (2013) suggested that strong undertow velocities can have a similar effect on the shear stress beneath shortwaves, although field observations to support this hypothesis are hitherto lacking.

Most of the above mentioned studies were conducted in flow tunnels, where the effects of nonlinear oscillatory flow on sand suspension are studied in isolation. In nature, however, these asymmetric oscillatory flows only exist in combination with breaking-induced turbulence injected from the water surface. This breaking-induced turbulence can descend toward the bed and enhance pickup and vertical mixing of sediment (e.g., Beach & Sternberg, 1996; Nadaoka et al., 1988; Sato et al., 1990; van der Zanden et al., 2017; Voulgaris & Collins, 2000). The effect of surface-induced turbulence on shortwave sand transport depends on whether the turbulent vortices reach the bed during the positive or the negative flow phase. This phase coupling between the surface-induced turbulence and the wave orbital motion was found to be positive under plunging breakers (e.g., Aagaard & Hughes, 2010; Brinkkemper et al., 2017; Ting & Kirby, 1995). However, under spilling breakers and bores, contradictory observations were described, with the phase coupling being positive (e.g., Ting & Kirby, 1994), negative (e.g., Ting & Kirby, 1996; Yoon & Cox, 2012), or absent (e.g., Aagaard & Hughes, 2010; van der Zanden et al., 2016).

Practical engineering models rely on empirical parameterizations of the sand transport, irrespective of the precise mechanisms responsible. In this study, we combine sand flux measurements at three distinct beach profiles and hypothesize that, in order to improve sand transport predictions in the surf zone, the velocity asymmetry could be used as a proxy to include the combined effect of the relevant transport mechanisms in the parameterizations. First, we introduce the three different data sets and discuss the data processing and analysis in section 2. In section 3 general trends in the measured shortwave sand flux are discussed and are combined to explain its relative contribution to the total flux. In section 4 we discuss the significance of our findings and suggest further steps to improve sand transport predictions in the shallow surf zone. Lastly, the main conclusions are summarized in section 5.

2. Methods

2.1. Data Collection

Observations used for this study were collected during two field and one large-scale wave flume experiments. The first field campaign took place on the gently sloping (1:80, Figure 1) Ballum beach at the Dutch barrier island Ameland (AM) in the autumn of 2010 (de Bakker et al., 2014). The second field campaign was conducted at the moderately sloping (1:35) Sand Engine (SE) beach, a meganourishment (de Schipper et al., 2016) near the town Ter Heijde, also in the Netherlands, in the autumn of 2014 (de Bakker et al., 2016). The flume measurements were collected on a steep beach profile (initially 1:15) during BD (Barrier Dynamics Experiment II) in the Delta Flume in the summer of 2012 (Masselink et al., 2016). The median sand grain size d_{50} was 200, 350, and 420 μm for AM, SE, and BD, respectively.

During the three studies, measurements of near-bed flow velocities, near-bed pressure, and sand concentrations were collected with instruments attached to four rigs deployed in a cross-shore array (Figure 1). Three of those rigs were equipped with an electromagnetic flowmeter, three optical backscatter sensors (Seapoint Turbidity Meters or STMs), and a pressure transducer (PT). The nominal height of the instruments above the

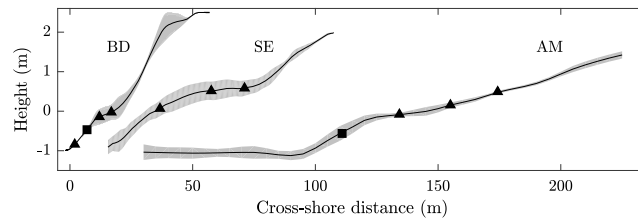


Figure 1. Mean cross-shore beach profiles with (gray) standard deviation during the experiments BARDEXII (BD), Sand Engine (SE) 2014, and Ameland (AM) 2010. The squares and triangles indicate the location of the rigs, of which the squares indicate the location of the rig with acoustic Doppler velocimeters.

bed was 0.15–0.20 m for the electromagnetic flowmeter, 0.03–0.20 m for the STMs (with a vertical spacing of ≈ 0.04 m between the sensors), and 0.05–0.10 m for the PT. The fourth rig comprised three vertically spaced acoustic Doppler velocimeters (ADV), seven STMs, and a PT. The nominal heights of these instruments were 0.15–0.70 m for the three ADVs (evenly spaced in the vertical), 0.04–0.70 m for the STMs (with a vertical spacing of 0.03 m between the lowest five STMs and ≈ 0.25 m between the highest three), and 0.05–0.10 m for the PT. The sampling frequency of all instruments was 4 Hz, except for the ADVs that sampled at 10 Hz. The data from the fourth rig at SE were discarded as large bed level changes affected the rig stability.

The cross-shore instrument array was located in the intertidal zone during the AM and SE field campaigns. This implies that the instruments were submerged and measuring during high tide, while data retrieval and adjustment of the sensor height were possible during low tide. Also during low tide, cross-shore bed profiles were measured with RTK-GPS every other day at AM and every day at SE. At SE, offshore wave conditions were obtained from a directional wave buoy located in 11-m water depth, 0.8 km seaward of the measurement array. For AM, these data were available from a directional wave buoy in 24-m water depth.

The BD experiments consisted of five test series (A–E) that were divided into tests with different wave and/or water level conditions. The tests were subsequently divided into wave runs with a duration of 10 to 120 min. The test series were run consecutively, without resetting the bed to its initial state. The bed level was surveyed after each wave run along the centerline of the flume (Ruessink et al., 2016). The vertical position of the instruments was then also adjusted, implying that the height of the instruments was identical at the start of each wave run.

2.2. Measurement Conditions

Offshore wave heights H_0 during the SE campaign were between 0.1 and 4.9 m with significant wave periods T_0 between 2.7 and 14.2 s (Figures 2a and 2d). The first 4 weeks of the campaign are characterized by low offshore wave heights ($H_0 < 0.5$ m) alternating with short periods with moderate wave heights of 1.5–2.0 m. A storm during the last week of the campaign resulted in H_0 up to 4.9 m and an elevated water level up to 2 m above mean sea level. Wave dissipation during high tide and seaward of the first measurement rig only occurred when the offshore wave height was larger than 1 m. The tidal range at the SE was around 2 m (Figure 2g).

The data from the BD experiment that focused on surf zone dynamics can be divided into six test series (A1–A4, A6–A8, B1, B2, C1, and C2). The wave height and peak wave period were 0.89 m and 8 s, respectively, for series A1–A4 (Figures 2b and 2e). Subsequently, the wave height was lowered to 0.75 m and the wave period increased to 12 s for A6–A8. The wave conditions during B1 and B2 are equal to A1–A4, but the water level was 0.5 m lower during B2 (Figure 2h). The water level was gradually raised from $\eta = 0$ to $\eta = 1.3$ m during C1 and lowered back to $\eta = 0$ m during C2 to simulate a full tidal cycle over a time span of 12 hr. The wave height was lowered to 0.55 m during the last wave runs of C1 and the first of C2 to avoid waves overtopping the flume walls.

H_0 during the field campaign at AM was generally higher than at SE but shows a similar range between 0.3 and 5.9 m (Figure 2c). T_0 ranged between 3.2 and 10.2 s and was higher during periods with large H_0 (Figure 2f). Wave heights were substantially reduced before reaching the first instrument rig, as wave breaking occurred on an ebb tidal delta a few kilometers offshore. The tidal range of 3 m is approximately 1 m higher than at SE (Figure 2i).

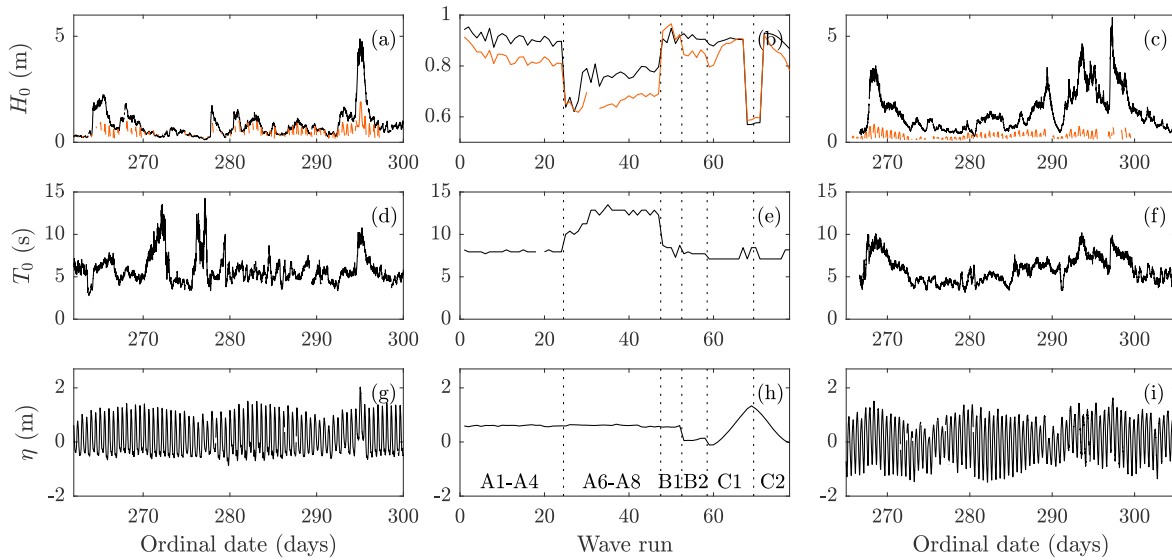


Figure 2. Wave characteristics and water levels during the lab and field experiments. (a–c) Significant wave height H_0 at (black) an offshore wave buoy or the wave maker and (red) the most seaward located suspension rig; (d–f) offshore significant wave period T_0 ; and (g–i) the water level η , for the (a, d, and g) Sand Engine, (b, e, and h) BARDEXII, and (c, f, and i) Ameland experiments.

2.3. Data Processing and Analysis

All data were initially analyzed in blocks of 30 min. The 30-min window was chosen as a sufficiently long period to attain a robust average over the typical wave characteristics, while it is short enough for the tidal water level to be approximately constant. Measured near-bed pressure was converted to sea surface elevation (η) with linear wave theory. The water depth (h) was calculated as the sum of the mean pressure and the instrument height above the bed. The significant high-frequency wave height (H_s) was calculated as the zeroth moment of the wave energy spectrum from 0.05 to 1 Hz.

The Ursell number was used to quantify the degree of nonlinearity (e.g., Doering & Bowen, 1995; Ruessink et al., 2012) and was calculated as

$$Ur = \frac{3}{4} \frac{a_w k}{(kh)^3}, \quad (1)$$

where $a_w = 0.5H_s$ and k is the wave number computed with linear theory using the peak wave period T_p .

The flow velocity was defined so that u is cross shore and positive in the landward direction. Subsequently, the cross-shore velocity was band-pass filtered into its low (u_{lf} , 0.005–0.05 Hz) and high (u_{hf} , 0.05–1 Hz) frequency component, that is, the long-wave and shortwave component. The nonlinearity of u_{hf} was expressed with its skewness S_u as

$$S_u = \frac{\langle u_{hf}^3 \rangle}{\langle u_{hf}^2 \rangle^{3/2}}, \quad (2)$$

where $\langle \dots \rangle$ denotes time averaging, and with its asymmetry A_u , by replacing u_{hf} in equation (2) with its Hilbert transform (Elgar, 1987). The velocity asymmetry is linearly correlated with the skewness of the acceleration but is less sensitive to the high-frequency cutoff that is used to estimate u_{hf} (Elgar, 1987).

The STMs were calibrated in a recirculation tank with sediment samples collected at the location of the instruments at the end of each campaign. The calibration resulted in a quadratic correlation between output voltages and concentration c up to ~ 30 – 40 kg/m³ with $r^2 \sim 0.99$ for all data sets. Field offsets that were present in the calibrated concentrations were determined from the cumulative frequency distribution (e.g., Aagaard & Hughes, 2006) and were around the 5th percentile for all STM data. These offsets were subtracted from the data, and negative values were set to 0.

STM measurements are sensitive to air bubbles (Puleo et al., 2006), and concentration time series collected in the surf zone should thus be checked for the presence of these bubbles. Air bubbles can be recognized

in concentration data as high and narrow spikes, often occurring prior to an actual sand suspension event. To diminish the effect of air bubbles on our analysis, concentration measurements were selected for the analysis based on two criteria: The sand concentration decreases vertically upward and a cross correlation with a higher sensor should show a positive correlation at a negative lag (Aagaard & Jensen, 2013); that is, events occur in general first at the lower sensor. Moreover, concentration time series that showed signs of the sensor being too close to the bed, or a fluctuating offset due to the presence of fine suspended particles, were rejected. Fluctuating offsets in the STM signals were particularly found in the SE data set during low-energetic conditions; hence, the block size in which data were quality controlled and analyzed for BD and AM (30 min) was reduced to 10 min for SE. This increased the number of blocks available for data analysis, as offsets were often approximately stable at a timescale of 10 min. A reduction in block length did not result in a wider range in conditions in the quality-controlled data for AM or BD, and it was thus decided to not reduce the block length for those data sets.

For each 10- or 30-min block that passed the concentration quality checks, the lowest STM in the range of 0.03–0.10 m above the bed was selected for further analysis. The concentration time series were frequency filtered into c_{hf} , c_{lf} and its mean component \bar{c} . These concentration components were combined with their correlating velocity components to calculate sand fluxes q_{tot} , q_{hf} , q_{lf} , and q_m at discrete sensor elevations as follows:

$$q_{tot} = q_{hf} + q_{lf} + q_m = \langle u_{hf} \cdot c_{hf} \rangle + \langle u_{lf} \cdot c_{lf} \rangle + \bar{u} \cdot \bar{c}, \quad (3)$$

where positive q means a flux in the shoreward direction and the angle brackets and overbar represent a time average. In this study, the term flux is used to refer to q at discrete sensor elevations, following the definition by Aagaard et al. (2013). The net suspended sand transport, which can be obtained by integrating q_{tot} over the vertical, could not be estimated here due to the low number of sensors in the vertical and their uncertain elevation above the bed during high tide at AM and SE. The relative contribution of q_{hf} to the total flux was calculated as follows:

$$\hat{q}_{hf} = \frac{q_{hf}}{|q_{hf}| + |q_{lf}| + |q_m|}. \quad (4)$$

The contributions of q_{lf} and q_m were calculated analogously as \hat{q}_{lf} and \hat{q}_m .

The height of the selected STM above the bed affects the measured mean concentration and can also affect the phase coupling between u and c . Phase lags in the vertical can be neglected for low-frequency motions (de Bakker et al., 2016) but are of importance at higher frequencies especially below nonbreaking waves above wave-induced ripples, which can reduce measured q_{hf} and even reverse the direction of the estimated flux (e.g., Van Der Werf et al., 2007). Beneath breaking waves, phase lags in the vertical are generally small (Brinkkemper et al., 2017). Here we explore the difference between \hat{q}_{hf} at the selected sensor and at a sensor 0.06 m higher in the water column (Figure 3) to avoid a sensitivity of the results to the height of the sensor. The difference between the two sensors can be explained by both a decreasing concentration and a decreasing phase coupling between u_{hf} and c_{hf} vertically upward; hence, \hat{q}_{hf} at +0.06 m is both above and below the line of perfect agreement with \hat{q}_{hf} at the selected sensor for SE (Figure 3a). Although \hat{q}_{hf} shows considerable sensitivity to sensor height above the bed for SE, fluxes are generally (in 88% of the data blocks) in the same direction. This is often not the case for BD (Figure 3b), where large phase lags between the sensors can result in a reversal of the flux direction. Brinkkemper et al. (2017) showed for the same data set that these phase lags particularly occur beneath nonbreaking waves with steep ripples. As our analysis focuses on breaking wave conditions, measurements are used in the following analysis only when the ripple steepness was below 0.05. This also reduces the sensitivity of our results to the height of the sensor above the bed. The normalized measurements collected in the inner-surf zone at AM are not sensitive to sensor height (Figure 3c). This lack of sensitivity indicates that the relatively small grain size at AM does not induce a phase lag between u_{hf} and c .

Quantile regression was used to test whether linear relations between hydrodynamic parameters and sand fluxes are statistically significant. This method is more robust than least squares regression when one or more factors of influence are unmeasured, that is, when data are scattered, as “outliers” affect least squares regression (Cade & Noon, 2003). Regression lines were computed for the minimum, median, and maximum

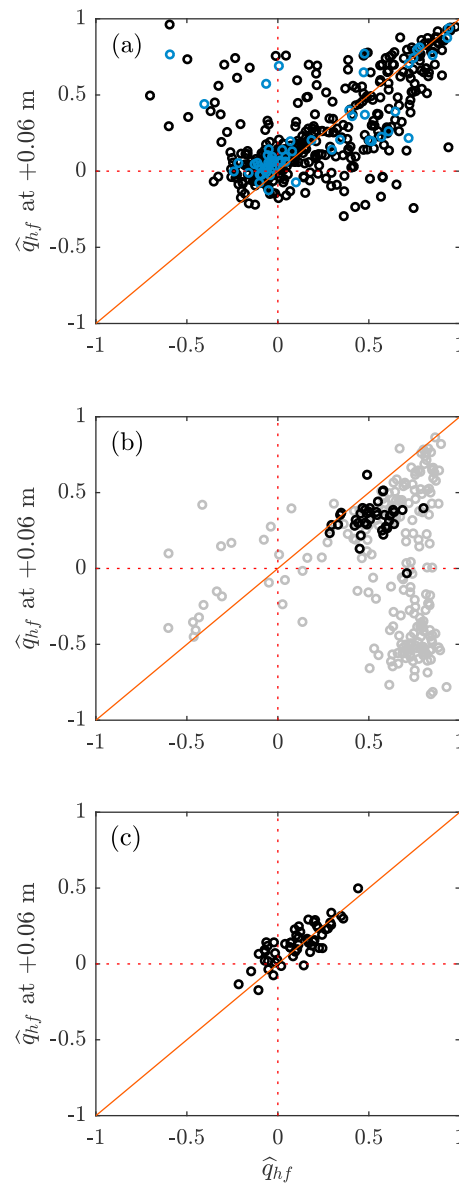


Figure 3. The relative contribution of q_{hf} for the total sand flux at the selected STM and at a sensor 0.06 m higher for the (a) Sand Engine, (b) BARDEXII, and (c) Ameland data sets. The red solid line is the line of equality. The blue and black circles in (a) signify the 30- and 10-min blocks, respectively. The black circles in (b) are observations that were selected for further analysis based on the ripple steepness. See section 2.3 for further explanation.

response by taking the 10%, 50%, and 90% quantiles, denoted as $\tau = 0.1, 0.5$, and 0.9 , following the approach of de Bakker et al. (2016). The 90% statistical significance of these regression lines was estimated following Koenker (2005).

2.4. Wave Nonlinearity

The wide range in offshore wave conditions resulted in a range in H_s/h at the different rigs for the selected time series. This range was $H_s/h = 0.18 - 0.81$, $H_s/h = 0.56 - 1.31$, and $H_s/h = 0.35 - 0.64$ for the SE, BD, and AM experiments, respectively. Considering the seaward boundary of the surf zone to be $H_s/h \sim 0.33$ for mild to moderately sloping beaches (Ruessink et al., 1998) and $H_s/h \sim 0.65$ for the steep beach slope in BD (Brinkkemper et al., 2016), the large majority of the measurements were collected in the surf zone (Figure 4). Due to the placement of the rigs in shallow water (h is typically between 0.5 and 1.5 m, except during the storm surge toward the end of the campaign at SE, when h is up to 3 m), this includes the outer- and inner-surf zone

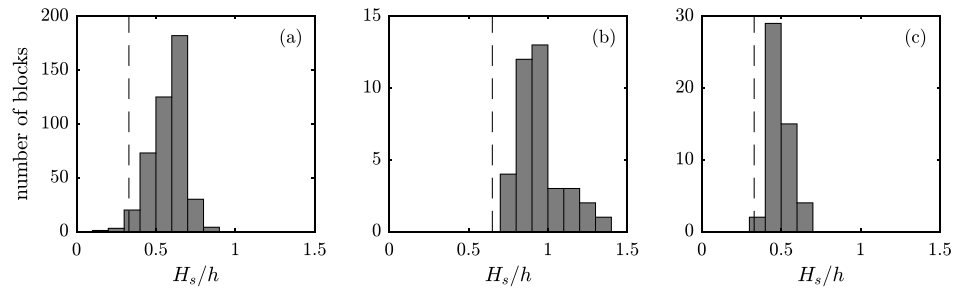


Figure 4. Histogram of the number of data blocks that include sand fluxes for the (a) Sand Engine, (b) BARDEXII, and (c) Ameland experiments, separated in 0.1 wide classes of relative wave height H_s/h . The vertical dashed line represents an estimate of H_s/h at the seaward edge of the surf zone.

during low-energetic conditions and only the inner-surf zone during high-energetic conditions. The term *shallow surf zone* is here used to refer to the hydrodynamic zone in which these measurements were collected.

The wide range in offshore wave height and periods at SE, together with a relatively high number of data blocks that passed the quality checks, resulted in observations collected beneath waves, which demonstrate a wide range in nonlinearity, from a near-sinusoidal wave orbital motion with $S_u \sim 0.2$ and $A_u \sim 0$ to a highly skewed/asymmetric wave orbital motion with $S_u \sim 1$ and $A_u \sim -1$ (Figure 5). The velocity skewness in the measured range does not show a clear dependence on Ur . The velocity asymmetry, however, increases with Ur until $Ur \gtrsim 10$, consistent with the parameterization by Ruessink et al. (2012; Figure 5a). While values for S_u for BD and AM are similar for equal Ur , A_u at BD is higher in comparison for the same Ur at AM.

3. Results

The observations from SE that passed the quality checks contained a wide range of hydrodynamic conditions, from low-energy swell to high-energy wind waves. Two high tides were selected from the SE data set as examples of accretive and erosive conditions (Figure 6): a high tide with low-energetic swell waves ($H_0 = 0.35$ m, $T_s = 9$ s) and a high tide with relatively energetic wind waves ($H_0 = 1.10$ m, $T_s = 5$ s), respectively. Fluxes at the selected sensor were averaged over a 2-hr block around each high tide to enable a comparison with the net morphological changes. The intertidal bar steepens and moves in the landward direction during the accretive high tide (Figure 6a). Moreover, a swash berm develops around the high water line. The magnitude

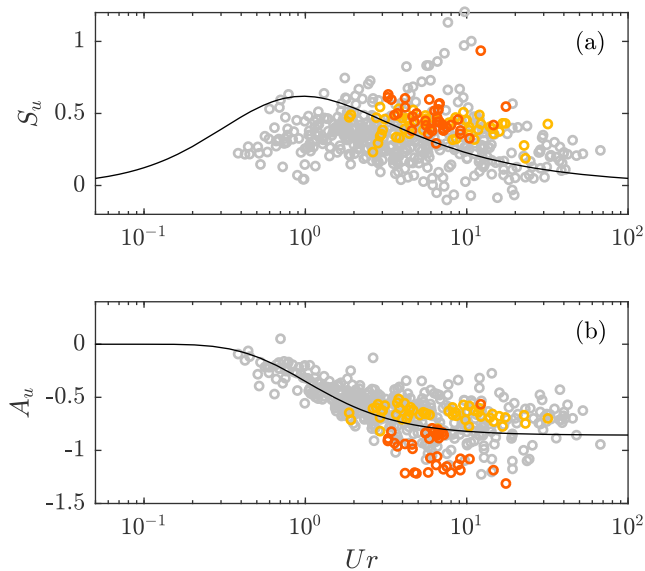


Figure 5. Velocity nonlinearity (a) velocity skewness S_u and (b) velocity asymmetry A_u versus the Ursell number Ur for the Sand Engine (gray), BARDEXII (red), and Ameland (yellow) experiments for cases where sand fluxes are available. The solid lines show parameterizations based on field data by Ruessink et al. (2012).

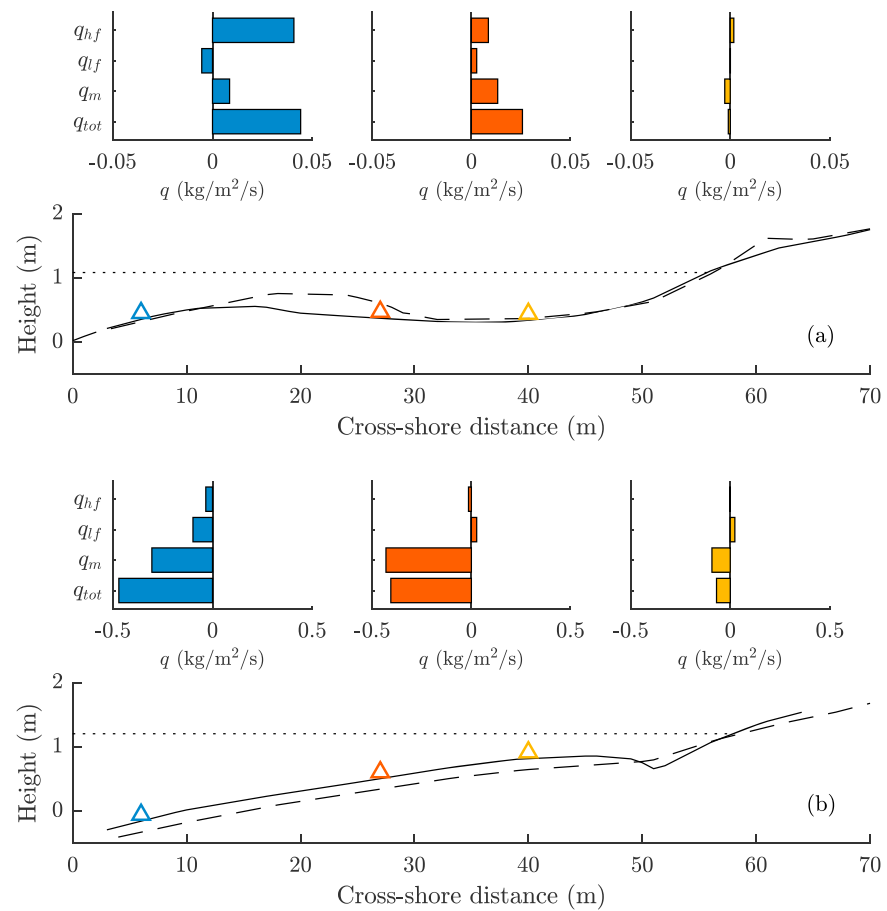


Figure 6. Sand fluxes at (triangles) three cross-shore locations for the Sand Engine experiment, averaged over (a) two accretive high tides and (b) two erosive high tides. Shown cases correspond to offshore wave conditions (a) $H_0 = 0.35$ m, $T_s = 9$ s and (b) $H_0 = 1.10$ m, $T_s = 5$ s. The solid (dashed) line shows the beach profile before (after) the high tides, and the dotted line shows the mean high tide water level. The bar plot colors correspond with the colors used to indicate the locations of the rigs.

of q_{hf} is largest on the seaward flank of the bar, where it dominates the total sand flux and decreases across the intertidal bar in the landward direction. The magnitude of q_{lf} is small but changes direction from offshore to onshore over the intertidal bar. This is caused by a change in correlation between the shortwave envelope, a proxy of sand stirring, and the long-wave orbital motion from negative to positive values, as shown by de Bakker et al. (2016) using the same SE data set. Mean cross-shore currents transport sand in the onshore direction above the intertidal bar. This indicates the presence of a horizontal cell circulation, with a mean current in the landward direction over the bar and presumably seaward flow in a nearby cross-shore-oriented channel. The onshore migration of the sandbar is thus mainly driven by cross-shore gradients in q_{hf} and q_m , with a small contribution of q_{lf} landward of the crest of the bar.

The intertidal beach is flattened and lowered during the erosive high tide (Figure 6b). Here q_{tot} is order of magnitude larger than during the accretive conditions and is directed offshore. The contribution of q_{hf} to q_{tot} is relatively small and is now in the offshore direction. The change in direction of q_{lf} over the intertidal bar, as observed during accretive conditions, is also apparent here. The flattening of the beach profile is, however, dominantly caused by the cross-shore gradient in the offshore-directed mean flux. These results show that gradients in the measured sand flux can be related qualitatively with morphological changes of the beach profile.

The contribution of the separate transport components q_{hf} , q_{lf} , and q_m to q_{tot} for all SE data is shown in Figure 7 versus H_0 . At the most seaward located rig, \hat{q}_{hf} is onshore directed and often dominates the total flux for $H_0 \lesssim 0.5$ m (blue circles in Figure 7a). With increasing offshore wave height, \hat{q}_{hf} decreases and the flux

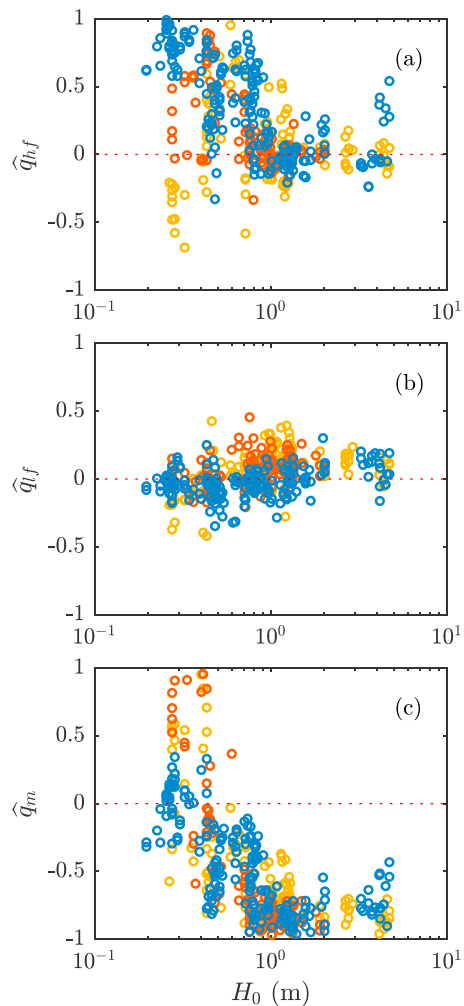


Figure 7. Contributions of the (a) shortwave flux q_{hf} , (b) long-wave flux q_{lf} , and (c) the mean flux q_m to the total flux ($|q_{hf}| + |q_{lf}| + |q_m|$) versus the offshore significant wave height H_0 in the SE data set. The colors indicate the location of the measurements with the (blue) most seaward located rig and (yellow) the most landward located rig.

direction becomes seaward. Observations at the two other rigs also follow this trend for high H_0 , but there is a dependency on cross-shore location when wave heights are low. This is explained by a larger heterogeneity in the cross-shore morphology, as the intertidal bar is more pronounced during these conditions. The contribution of q_{lf} can be both positive and negative and rarely exceeds 20% of the total flux. As q_{hf} and q_m explain the bulk of the sand fluxes, $|q_m|$ is low when $|q_{hf}|$ is high and vice versa. The total flux is dominated by q_m when $H_0 \gtrsim 1$ m. The above mentioned cell circulation, and thus a shoreward directed mean current over the bar, was observed during conditions with low H_0 only.

For the low-energetic conditions in the SE data set when q_{hf} dominates the total suspended flux, that is, for $H_0 < 0.5$ m, the magnitude of the flux is related to wave characteristics. q_{hf} is largest beneath waves with high root-mean-square orbital velocity (u_{rms} , calculated from u_{hf}) and high A_u (Figures 8a and 8b). Quantile regression of q_{hf} with A_u gives significant increasing trends for quantiles 0.5 and 0.9, while the magnitude of q_{hf} is unrelated to A_u for $\tau = 0.1$. The absence of a significant increasing trend for the lowest quantile can be explained by the relatively low q_{hf} measured at the rig located in the trough between the intertidal bar and the shoreline. Interestingly, S_u , which is commonly used to predict q_{hf} (e.g., van Rijn, 2007), is not correlated with the magnitude of q_{hf} in these surf zone measurements (Figure 8c). With all wave conditions included, the magnitude of q_{hf} is related with \bar{u} (Figure 8d). The downward trend of q_{hf} with increasing seaward directed \bar{u} is significant for quantiles $\tau = 0.1$ and $\tau = 0.5$. This trend is probably related to the offshore-directed mean current increasing the flow velocity during the seaward directed phase of the orbital motion and decreasing

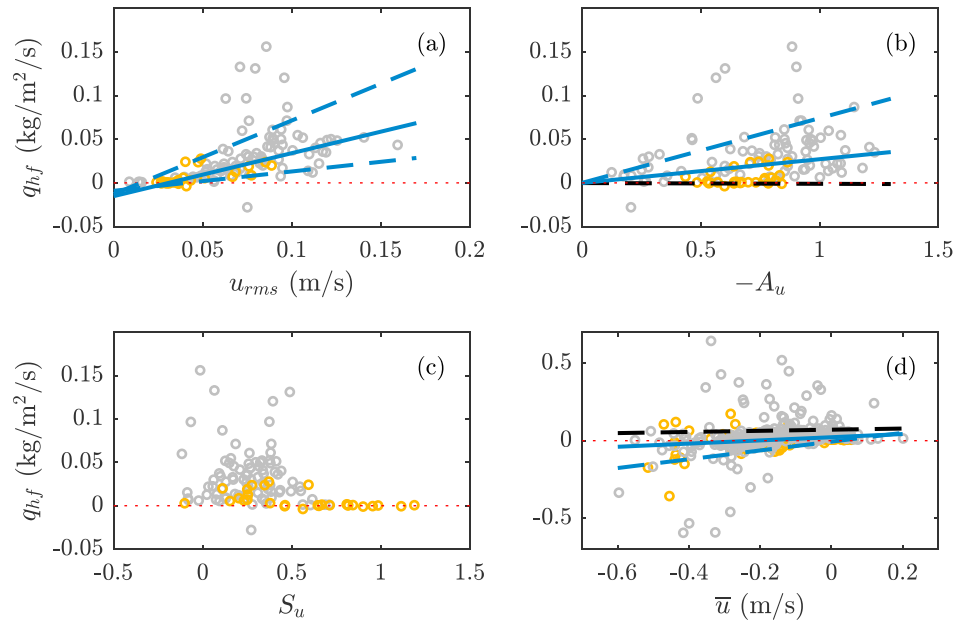


Figure 8. Shortwave flux q_{hf} versus (a) root-mean-square orbital velocity u_{rms} , (b) velocity asymmetry $-A_u$, (c) velocity skewness S_u , and (d) mean cross-shore current \bar{u} . In (a)–(c) only low-energetic conditions ($H_0 < 0.5$ m) are included; (d) contains all data. Measurements at the most landward located rig are emphasized in yellow. Lines indicate regression over the (dashed) 0.1, (solid) 0.5 and (dashed), 0.9 percentiles and are blue when the slope is statistically significant.

the velocity during the landward directed phase. These results indicate that u_{rms} and A_u are positively correlated with the magnitude of the onshore-directed flux by shortwaves, while this flux reduces for increasing offshore-directed \bar{u} .

These insights from the SE data set are applied to scale the normalized q_{hf} for all conditions and to combine the SE data with those of BD and AM. Observations at the most landward SE rig were excluded, as it was often located in the trough between the intertidal bar and the upper beach where fluxes were often minute (Figure 6). Furthermore, only observations with offshore-directed \bar{u} were included. The interpretation of trends in \hat{q}_{hf} is complicated as it also includes q_{lf} and $q_{m'}$, of which the latter is obviously also related to \bar{u} . Scatter in the data due to variations in q_{lf} was omitted here by normalizing q_{hf} as $q_{hf}/(|q_{hf}| + |q_m|)$. Observations of $q_{hf}/(|q_{hf}| + |q_m|)$ were subsequently plotted versus $|\bar{u}|$ (Figure 9a) to investigate how much of its variability is explained by \bar{u} . The SE data show the full range between q_{hf} dominating over q_m [$q_{hf}/(|q_{hf}| + |q_m|) \sim 1$] and q_{hf} being of minor importance and in the offshore direction [$q_{hf}/(|q_{hf}| + |q_m|) \sim -0.1$], as was shown in Figure 7a. The range in magnitude of the mean cross-shore current for BD and AM is small and $\bar{u} \sim -0.15$ m/s. The contribution of q_{hf} to the total flux is, however, higher at BD, with $q_{hf}/(|q_{hf}| + |q_m|)$ between 0.4 and 0.9, with a mean of 0.60, versus $q_{hf}/(|q_{hf}| + |q_m|)$ between -0.2 and 0.4 , with a mean of 0.11, at AM (Figure 9a). When u_{rms} is included as $u_{rms}/|\bar{u}|$ (Figure 9b), scatter reduces. The data from BD and AM are now

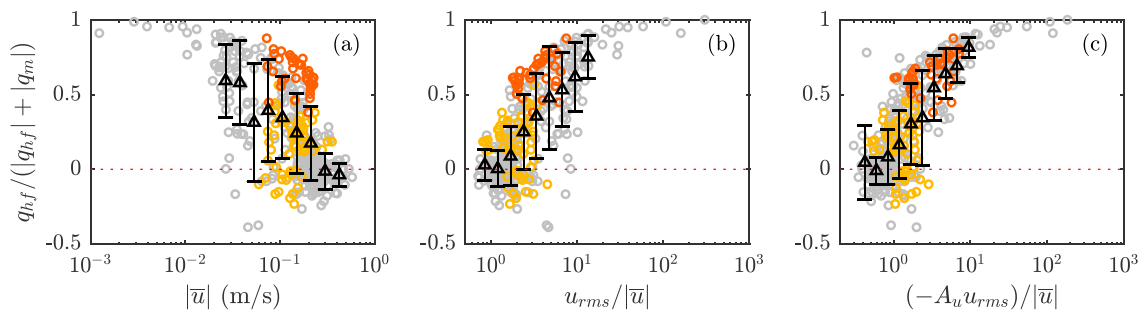


Figure 9. Normalized q_{hf} as $q_{hf}/(|q_{hf}| + |q_m|)$ at the selected Seapoint Turbidity Meter versus (a) $|\bar{u}|$, (b) $u_{rms}/|\bar{u}|$, and (c) $(-A_u u_{rms})/|\bar{u}|$ for the Sand Engine (gray), BARDEXII (red), and Ameland (yellow) experiments. The triangles show mean values with standard deviation for the data in bins with a bin width of 0.15 on the log axis.

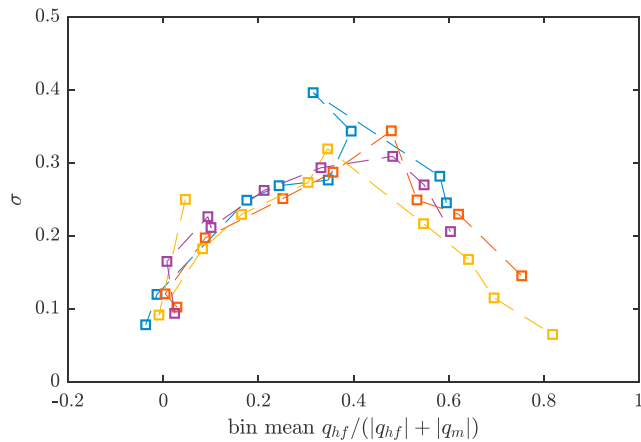


Figure 10. The standard deviation σ of the bins in Figure 9 versus the mean of the bins for $|\bar{u}|$ (blue), $u_{rms}/|\bar{u}|$ (red), $(-A_u u_{rms})/|\bar{u}|$ (yellow), and $(S_u u_{rms})/|\bar{u}|$ (purple).

also more separated on the x axis. This is explained by the relatively large u_{rms} for BD in comparison with AM: The mean $u_{rms}/|u|$ for BD is 3.91 versus 2.13 for AM. The scatter in the data is further reduced by adding A_u as $(-A_u u_{rms})/|\bar{u}|$ (Figure 9c), particularly where $q_{hf}/(|q_{hf}| + |q_m|) > 0.5$.

To illustrate the trends and scatter, the mean and standard deviation (σ) in $q_{hf}/(|q_{hf}| + |q_m|)$ were calculated in bins with a width of $\log_{10}(x) = 0.15$, where x represents the variables on the x axis in Figure 9. Bins were only included in the analysis if they contained more than 10 measurements. While σ for $|\bar{u}|$ and $u_{rms}/|\bar{u}|$ is very similar when the bin mean is $q_{hf}/(|q_{hf}| + |q_m|) < 0.4$, σ is smaller when u_{rms} is included for $q_{hf}/(|q_{hf}| + |q_m|) > 0.5$ (Figure 10). The reduced scatter in the data for $(-A_u u_{rms})/|\bar{u}|$ is also apparent from σ , as σ is lower for all bins with a bin mean $q_{hf}/(|q_{hf}| + |q_m|) > 0.5$. Furthermore, there is a wider range in the mean values of the bins for $(-A_u u_{rms})/|\bar{u}|$, and the data are thus better separated. Including S_u instead of $-A_u$ does not result in lower values for σ (Figure 10). Moreover, measurements with a high $q_{hf}/(|q_{hf}| + |q_m|)$ are not well separated from conditions with lower values, as the maximum bin mean is only 0.6. A_u is thus more

successful than S_u in predicting when the shortwave suspended sand flux dominates over the mean flux in the shallow surf zone. While including wave characteristics u_{rms} and A_u improves the predictability for $q_{hf} > -q_m$, the spread in the data remains when q_m dominates the suspended sand flux.

4. Discussion

The shortwave suspended sand flux, measured in the shallow surf zone under a wide variety of wave conditions and on a variety of beaches, was shown to increase with u_{rms} and A_u and to decrease with an increasing offshore-directed \bar{u} . The dependency on the wave characteristics u_{rms} and A_u was most apparent when $q_{hf} > -q_m$. This is particularly the case for low-energetic conditions during the SE field campaign, when long-period swell waves transformed into highly asymmetric plunging breakers in shallow water. These conditions are typically related with an onshore-directed propagation of the intertidal bar (Figure 6; Masselink et al., 2006; Aagaard et al., 2013). Elgar et al. (2001) previously discussed field measurements that showed the cross-shore maximum in velocity asymmetry to be consistently colocated with the crest of an onshore migrating bar and argued that A_u instead of S_u is driving the onshore migration. The sand flux measurements presented here confirm their hypothesis that, as long as the mean cross-shore current is weak, the onshore-directed shortwave flux in the shallow surf zone is more closely related with A_u than S_u . Under more energetic conditions, when the net sand flux becomes offshore directed, the magnitude and direction of the shortwave sand flux also depend on the magnitude of the offshore-directed mean current. This is explained by the opposing current causing an increase in shear stress during the negative flow phase and a decrease in shear stress during the positive flow phase of the waves. This effect was earlier measured for shear waves (Miles et al., 2002), infragravity waves (de Bakker et al., 2016), and oscillatory flows (Ruessink et al., 2011).

The wave-driven suspended sand transport in morphodynamic models is often based on empirical parameterizations including the near-bed wave orbital motion and the velocity skewness (e.g., van Rijn, 2007). These parameterizations include calibration coefficients that are site specific (e.g., Dubarbarier et al., 2015; Nienhuis et al., 2016; Walstra et al., 2015), and optimal settings for deeper water are not necessarily optimal for shallow water and vice versa (Ruggiero et al., 2009). This implies that certain physical processes are either misrepresented or lacking in the transport formulations. The measurements presented in this study show that, in the shallow surf zone, A_u is more closely related with the shortwave-driven suspended sand flux than S_u . Including A_u in empirical transport parameterizations could thus improve the performance of morphodynamic models in shallow water. The suitability of A_u to predict the wave-driven sand transport in the shallow surf zone, in contrast to S_u explaining more of the transport in the shoaling and outer surf zone, was also suggested using numerical models (Hoefel & Elgar, 2003; Calantoni & Puleo, 2006; Fernández-Mora et al., 2015). These studies showed that the inclusion of a sand transport proxy based on the velocity asymmetry improved the model ability to reproduce measured onshore sandbar migration.

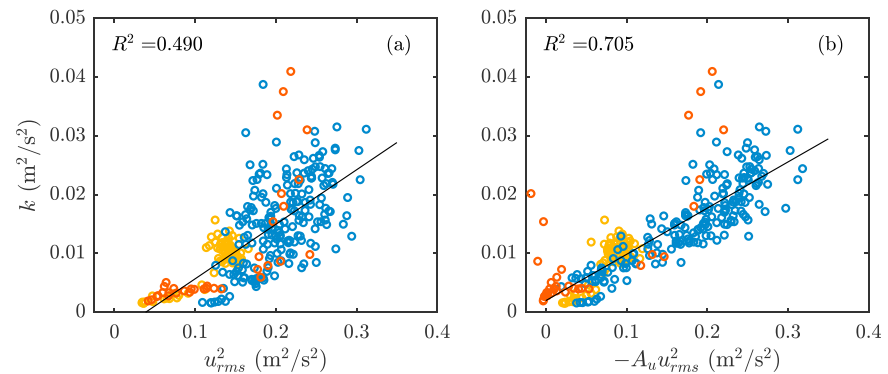


Figure 11. Measured turbulent kinetic energy k between 0.1 and 0.5 m above the bed versus (a) u_{rms}^2 and (b) $-A_u u_{rms}^2$ during laboratory experiment BARDEXII (red), and field campaigns at Truc Vert beach (blue), and Ameland (yellow).

The onshore transport by velocity asymmetric flows has been explained by a variety of factors: acceleration skewness (e.g., Austin et al., 2009), phase lags (e.g., Grasso et al., 2011; Ruessink et al., 2011), boundary layer thickness (Nielsen, 1992), horizontal pressure gradients (e.g., Calantoni & Puleo, 2006; Foster et al., 2006; Sleath, 1999), and breaking-induced turbulence (e.g., van Thiel de Vries et al., 2008; see also section 1). It is thus not necessarily the velocity asymmetry that is driving the onshore wave-induced transport but rather a combination of processes that are connected to and scale with A_u . To illustrate that, for example, the turbulent kinetic energy k in the water column scales with $A_u u_{rms}^2$, k was estimated from velocity measurements collected during BD (Brinkkemper et al., 2016), AM (Grasso & Ruessink, 2012), and a field campaign at Truc Vert beach (France) in 2008 (Grasso & Ruessink, 2012; Ruessink, 2010). As mentioned in section 2, these measurements could not be collected at SE. During these campaigns, horizontal and vertical flow velocities were measured using three vertically spaced ADVs. The turbulent velocities were extracted from these measurements using the differencing method (Feddersen & Williams, 2007; see Brinkkemper et al., 2016, for further details on the data processing). Here data were selected when instruments were between 0.1 and 0.5 m above the bed. These data show a linear correlation of k with $-A_u u_{rms}^2$ ($R^2 = 0.705$, Figure 11b); this correlation is stronger than that for u_{rms}^2 alone ($R^2 = 0.490$, Figure 11a). Whether surface-induced turbulence beneath surf bores reaches the bed dominantly during the positive or the negative phase of the wave orbital motion, crucial in order to affect q_{hf} , is not yet clear.

The identification of the impact of the individual processes related to A_u is not necessarily needed to improve transport formulations in practical engineering models, as these models rely largely on empirical parameterizations. Parameterizations based on A_u could be developed to include the combined effect of these processes, including the effect of breaking-induced turbulence. A first step would be to improve parameterizations to accurately predict A_u itself, as the difference in A_u between AM and BD cannot be predicted (Figure 5b) using conventional parameterizations based on U_r (Doering & Bowen, 1995; Ruessink et al., 2012). The solution might be to include offshore wave steepness and/or the beach slope to make the parameterizations broader applicable, as was recently suggested by Rocha et al. (2017).

The effectiveness of velocity asymmetric flows to induce sand mobilization and transport was earlier found to depend on sediment grain size (e.g., Ruessink et al., 2009; Shimamoto et al., 2013; van der A et al., 2010), although a positive correlation between the velocity asymmetry and the shortwave transport exists for a wide range in grain sizes (van der A et al., 2010). The data used in this study were collected on beaches consisting of sand with a d_{50} of (AM) 200, (SE) 350, and (BD) 420 μm . While the range in sediment sizes could explain part of the remaining scatter in Figure 9, the inclusion of A_u in the parameterization does reduce scatter both between the SE and BD data sets as well as within the SE data set. It can therefore be argued that the reduction in scatter cannot be explained solely by the difference in grain size between the data sets. It is not possible to determine whether this is also true for the smaller grain size at AM, as the measured fluxes were all in the range $|q_m| > q_{hf}$, where the inclusion of A_u does not result in a better representation of $q_{hf}/(|q_{hf}| + |q_m|)$.

5. Conclusions

Near-bed suspended sand fluxes, collected in the shallow surf zone of a moderately sloping natural beach (SE), ranged from onshore directed and shortwave dominated under low-energetic conditions ($H_0 \lesssim 0.5$ m) to offshore directed and dominated by mean cross-shore currents under high-energetic conditions ($H_0 \gtrsim 0.8$ m). Cross-shore gradients in these suspended sand fluxes correlate with morphological changes, and the fluxes thus relate qualitatively with the total vertically integrated sand transport.

The onshore-directed shortwave sand flux during low-energetic conditions is highest beneath larger asymmetric waves and is not correlated with velocity skewness. Shortwave fluxes over the full range of conditions at SE show a correlation with the magnitude of the mean cross-shore current. The shortwave suspended sand flux reduces and reverses direction with an increase in the offshore-directed current. These correlations suggest the shortwave flux in the shallow surf zone increases with u_{rms} and A_u and decreases with increasing offshore-directed \bar{u} .

Data sets collected in the shallow surf zone of a mildly sloping natural beach (AM) and a steep laboratory beach (BD) were included to further investigate these correlations. The normalized shortwave flux $q_{hf}/(|q_{hf}| + |q_m|)$ scales with $u_{rms}/|\bar{u}|$ for the combination of the three data sets. This relation is further improved for $q_{hf} > |q_m|$ by including the velocity asymmetry. The inclusion of velocity skewness, a parameter often linked with shortwave sand transport in the shoaling zone, did not improve the results. We hypothesize that the velocity asymmetry is a good proxy for the combined effect of several transport mechanisms that were shown to be of importance in the shallow surf zone in earlier studies, for example, acceleration skewness, horizontal pressure gradients, and breaking-induced turbulence. These sand flux measurements thus support the hypothesis that the inclusion of velocity asymmetry in sand transport parameterizations, as proxy for the shortwave sand transport, will improve the performance of morphodynamic models in shallow water, especially for onshore sandbar migration and beach recovery during low-energy wave conditions.

Acknowledgments

The hydrodynamical and sand flux data are available from the Dryad Digital Repository: <https://doi.org/10.5061/dryad.tn70pf1>. We gratefully acknowledge the technical support of Henk Markies, Marcel van Maarseveen, and Chris Roosendaal and the help of Aline Pieterse, Emily McCullough, Jantien Rutten, Marieke Dirksen, Florian van der Steen, Laura Brakenhoff, Daan Wesselman, Winnie de Winter, and Florent Grasso during the field and laboratory campaigns. The discussions with Jantien Rutten, Timothy Price, and Drude Fritzboeger Christensen helped to compose this work further. Furthermore, we thank the three reviewers for their valuable comments on the manuscript. J. A. B. and B. G. R. were funded by the Dutch Technology Foundation STW, which is part of the Netherlands Organisation for Scientific Research (NWO), and are partly funded by the Ministry of Economic Affairs (project 12397). T. A. was funded by the Danish Natural Sciences Research Council, grant 4181-00045. A. T. M. d. B. was funded by the Chaire Regional Program EVEX and a PRESTIGE incoming mobility grant, cofinanced by the FP7 Marie Curie Actions-COFUND (grant agreement PCOFUND-GA-2013-609102).

References

- Aagaard, T., & Hughes, M. G. (2006). Sediment suspension and turbulence in the swash zone of dissipative beaches. *Marine Geology*, 228(1–4), 117–135. <https://doi.org/10.1016/j.margeo.2006.01.003>
- Aagaard, T., & Hughes, M. G. (2010). Breaker turbulence and sediment suspension in the surf zone. *Marine Geology*, 271(3–4), 250–259. <https://doi.org/10.1016/j.margeo.2010.02.019>
- Aagaard, T., & Jensen, S. G. (2013). Sediment concentration and vertical mixing under breaking waves. *Marine Geology*, 336, 146–159. <https://doi.org/10.1016/j.margeo.2012.11.015>
- Aagaard, T., Black, K. P., & Greenwood, B. (2002). Cross-shore suspended sediment transport in the surf zone: A field-based parameterization. *Marine Geology*, 185(3), 283–302. [https://doi.org/10.1016/S0025-3227\(02\)00193-7](https://doi.org/10.1016/S0025-3227(02)00193-7)
- Aagaard, T., Greenwood, B., & Hughes, M. (2013). Sediment transport on dissipative, intermediate and reflective beaches. *Earth-Science Reviews*, 124, 32–50. <https://doi.org/10.1016/j.earscirev.2013.05.002>
- Austin, M., Masselink, G., O'Hare, T., & Russell, P. (2009). Onshore sediment transport on a sandy beach under varied wave conditions: Flow velocity skewness, wave asymmetry or bed ventilation? *Marine Geology*, 259(1), 86–101. <https://doi.org/10.1016/j.margeo.2009.01.001>
- Beach, R. A., & Sternberg, R. W. (1996). Suspended-sediment transport in the surf zone: Response to breaking waves. *Continental Shelf Research*, 16(15), 1989–2003.
- Brinkkemper, J. A., Lanckriet, T., Grasso, F., Puleo, J. A., & Ruessink, B. G. (2016). Observations of turbulence within the surf and swash zone of a field-scale sandy laboratory beach. *Coastal Engineering*, 113, 62–72. <https://doi.org/10.1016/j.coastaleng.2015.07.006>
- Brinkkemper, J. A., de Bakker, A. T. M., & Ruessink, B. G. (2017). Intrawave sand suspension in the shoaling and surf zone of a field-scale laboratory beach. *Journal of Geophysical Research: Earth Surface*, 122, 356–370. <https://doi.org/10.1002/2016JF004061>
- Cade, B. S., & Noon, B. R. (2003). A gentle introduction to quantile regression for ecologists. *Frontiers in Ecology and the Environment*, 1(8), 412–420. [https://doi.org/10.1890/1540-9295\(2003\)001\[0412:AGITQR\]2.0.CO;2](https://doi.org/10.1890/1540-9295(2003)001[0412:AGITQR]2.0.CO;2)
- Calantoni, J., & Puleo, J. A. (2006). Role of pressure gradients in sheet flow of coarse sediments under sawtooth waves. *Journal of Geophysical Research*, 111, C01010. <https://doi.org/10.1029/2005JC002875>
- de Bakker, A. T. M., Tissier, M. F. S., & Ruessink, B. G. (2014). Shoreline dissipation of infragravity waves. *Continental Shelf Research*, 72, 73–82. <https://doi.org/10.1016/j.csr.2013.11.013>
- de Bakker, A. T. M., Brinkkemper, J. A., Steen, F., Tissier, M. F. S., & Ruessink, B. G. (2016). Cross-shore sand transport by infragravity waves as a function of beach steepness. *Journal of Geophysical Research: Earth Surface*, 121, 1786–1799. <https://doi.org/10.1002/2016JF003878>
- de Schipper, M. A., de Vries, S., Ruessink, G., de Zeeuw, R. C., Rutten, J., van Gelder-Maas, C., & Stive, M. J. (2016). Initial spreading of a mega feeder nourishment: Observations of the Sand Engine pilot project. *Coastal Engineering*, 111, 23–38.
- Doering, J., & Bowen, A. (1995). Parametrization of orbital velocity asymmetries of shoaling and breaking waves using bispectral analysis. *Coastal Engineering*, 26(1–2), 15–33. [https://doi.org/10.1016/0378-3839\(95\)00007-X](https://doi.org/10.1016/0378-3839(95)00007-X)
- Dubarbier, B., Castelle, B., Marieu, V., & Ruessink, G. (2015). Process-based modeling of cross-shore sandbar behavior. *Coastal Engineering*, 95, 35–50. <https://doi.org/10.1016/j.coastaleng.2014.09.004>
- Elgar, S. (1987). Relationships involving third moments and bispectra of a harmonic process. *IEEE Transactions on Acoustics, Speech, and Signal Processing*, 35(12), 1725–1726.
- Elgar, S., Gallagher, E. L., & Guza, R. (2001). Nearshore sandbar migration. *Journal of Geophysical Research*, 106, 11,623–11,627. <https://doi.org/10.1029/2000JC000389>

- Feddersen, F., & Williams, A. J. (2007). Direct estimation of the Reynolds stress vertical structure in the nearshore. *Journal of Atmospheric and Oceanic Technology*, 24(1), 102–116. <https://doi.org/10.1175/JTECH1953.1>
- Fernández-Mora, A., Calvete, D., Falqués, A., & Swart, H. (2015). Onshore sandbar migration in the surf zone: New insights into the wave-induced sediment transport mechanisms. *Geophysical Research Letters*, 42, 2869–2877. <https://doi.org/10.1002/2014GL063004>
- Foster, D., Bowen, A., Holman, R. A., & Natto, P. (2006). Field evidence of pressure gradient induced incipient motion. *Journal of Geophysical Research*, 111, C05004. <https://doi.org/10.1029/2004JC002863>
- Grasso, F., & Ruessink, B. G. (2012). Turbulent viscosity in natural surf zones. *Geophysical Research Letters*, 39, L23603. <https://doi.org/10.1029/2012GL054135>
- Grasso, F., Michallet, H., & Barthélemy, E. (2011). Sediment transport associated with morphological beach changes forced by irregular asymmetric, skewed waves. *Journal of Geophysical Research*, 116, C03020. <https://doi.org/10.1029/2010JC006550>
- Henderson, S. M., Allen, J. S., & Newberger, P. (2004). Nearshore sandbar migration predicted by an eddy-diffusive boundary layer model. *Journal of Geophysical Research*, 109, C06024. <https://doi.org/10.1029/2003JC002137>
- Hoefel, F., & Elgar, S. (2003). Wave-induced sediment transport and sandbar migration. *Science*, 299(5614), 1885–1887. <https://doi.org/10.1126/science.1081448>
- King, D. B. (1991). Studies in oscillatory flow bedload sediment transport (PhD thesis), University of California, San Diego.
- Koenker, R. (2005). *Quantile regression*. UK: Cambridge University Press.
- Masselink, G., Kroon, A., & Davidson-Arnott, R. (2006). Morphodynamics of intertidal bars in wave-dominated coastal settings—A review. *Geomorphology*, 73(1), 33–49. <https://doi.org/10.1016/j.geomorph.2005.06.007>
- Masselink, G., Ruju, A., Conley, D., Turner, I., Ruessink, G., Matias, A., et al. (2016). Large-scale barrier dynamics experiment II (BARDEX II): Experimental design, instrumentation, test programme and data set. *Coastal Engineering*, 113, 3–18. <https://doi.org/10.1016/j.coastaleng.2015.07.009>
- Miles, J., Russell, P., Ruessink, B., & Huntley, D. (2002). Field observations of the effect of shear waves on sediment suspension and transport. *Continental Shelf Research*, 22(4), 657–681. [https://doi.org/10.1016/S0278-4343\(01\)00095-4](https://doi.org/10.1016/S0278-4343(01)00095-4)
- Nadaoka, K., Ueno, S., & Igarashi, T. (1988). Sediment suspension due to large scale eddies in the surf zone. In *Proceedings of the 21st International Conference on Coastal Engineering* (pp. 1646–1660). Malaga, Spain.
- Nielsen, P. (1992). Coastal bottom boundary layers and sediment transport, Advanced Series on Ocean Engineering, World Scientific.
- Nienhuis, J. H., Ashton, A. D., Nardin, W., Fagherazzi, S., & Giosan, L. (2016). Alongshore sediment bypassing as a control on river mouth morphodynamics. *Journal of Geophysical Research: Earth Surface*, 121, 664–683. <https://doi.org/10.1002/2015JF003780>
- O'Donoghue, T., & Wright, S. (2004). Flow tunnel measurements of velocities and sand flux in oscillatory sheet flow for well-sorted and graded sands. *Coastal Engineering*, 51(11–12), 1163–1184. <https://doi.org/10.1016/j.coastaleng.2004.08.001>
- Osborne, P. D., & Greenwood, B. (1992). Frequency dependent cross-shore suspended sediment transport. 2. A barred shoreface. *Marine Geology*, 106(1–2), 25–51.
- Puleo, J. A., Johnson, R. V., Butt, T., Kooney, T. N., & Holland, K. T. (2006). The effect of air bubbles on optical backscatter sensors. *Marine Geology*, 230(1), 87–97. <https://doi.org/10.1016/j.margeo.2006.04.008>
- Ribberink, J. S., & Al-Salem, A. A. (1994). Sediment transport in oscillatory boundary layers in cases of rippled beds and sheet flow. *Journal of Geophysical Research*, 99(C6), 12,707–12,727.
- Rocha, M., Michallet, H., & Silva, P. (2017). Improving the parameterization of wave nonlinearities—The importance of wave steepness, spectral bandwidth and beach slope. *Coastal Engineering*, 121, 77–89. <https://doi.org/10.1016/j.coastaleng.2016.11.012>
- Roelvink, J. A., & Stive, M. J. F. (1989). Bar-generating cross-shore flow mechanisms on a beach. *Journal of Geophysical Research*, 94(C4), 4785–4800. <https://doi.org/10.1029/JC094iC04p04785>
- Ruessink, B. G. (2010). Observations of turbulence within a natural surf zone. *Journal of Physical Oceanography*, 40(12), 2696–2712. <https://doi.org/10.1175/2010JPO4466.1>
- Ruessink, B. G., Houwman, K. T., & Hoekstra, P. (1998). The systematic contribution of transporting mechanisms to the cross-shore sediment transport in water depths of 3 to 9 m. *Marine Geology*, 152, 295–324.
- Ruessink, B. G., van den Berg, T. J. J., & van Rijn, L. C. (2009). Modeling sediment transport beneath skewed asymmetric waves above a plane bed. *Journal of Geophysical Research*, 114, C11021. <https://doi.org/10.1029/2009JC005416>
- Ruessink, B. G., Michallet, H., Abreu, T., Sancho, F., van der A, D. A., van der Werf, J. J., & Silva, P. A. (2011). Observations of velocities, sand concentrations, and fluxes under velocity-asymmetric oscillatory flows. *Journal of Geophysical Research*, 116, C03004. <https://doi.org/10.1029/2010JC006443>
- Ruessink, B. G., Ramaekers, G., & van Rijn, L. C. (2012). On the parameterization of the free-stream non-linear wave orbital motion in nearshore morphodynamic models. *Coastal Engineering*, 65(0), 56–63. <https://doi.org/10.1016/j.coastaleng.2012.03.006>
- Ruessink, B. G., Blenkinsopp, C., Brinkkemper, J. A., Castelle, B., Durbarbarier, B., Grasso, F., et al. (2016). Sandbar and beachface evolution on a prototype coarse-grained sandy barrier. *Coastal Engineering*, 113, 19–32. <https://doi.org/10.1016/j.coastaleng.2015.11.005>
- Ruggiero, P., Walstra, D. J. R., Gelfenbaum, G., & van Ormondt, M. (2009). Seasonal-scale nearshore morphological evolution: Field observations and numerical modeling. *Coastal Engineering*, 56(11–12), 1153–1172. <https://doi.org/10.1016/j.coastaleng.2009.08.003>
- Sato, S., Homma, K., & Shibayama, T. (1990). Laboratory study on sand suspension due to breaking waves. *Coastal Engineering in Japan*, 33(2), 219–231.
- Scott, N. V., Hsu, T.-J., & Cox, D. (2009). Steep wave, turbulence, and sediment concentration statistics beneath a breaking wave field and their implications for sediment transport. *Continental Shelf Research*, 29(20), 2303–2317. <https://doi.org/10.1016/j.csr.2009.09.008>
- Shimamoto, T., Nielsen, P., & Baldock, T. (2013). Updated “grab and dump” model for sediment transport under acceleration skewed waves. In *Proc. Seventh Int. Conf. on Coastal Dynamics* (pp. 1495–1504). Bordeaux, France: Bordeaux University.
- Silva, P. A., Abreu, T., Der, D. A., Sancho, A., Ruessink, B., Van der Werf, J., & Ribberink, J. S. (2011). Sediment transport in nonlinear skewed oscillatory flows: Transkew experiments. *Journal of Hydraulic Research*, 49, 72–80. <https://doi.org/10.1080/00221686.2011.592681>
- Sleath, J. (1999). Conditions for plug formation in oscillatory flow. *Continental Shelf Research*, 19(13), 1643–1664. [https://doi.org/10.1016/S0278-4343\(98\)00096-X](https://doi.org/10.1016/S0278-4343(98)00096-X)
- Ting, F. C. K., & Kirby, J. T. (1994). Observation of undertow and turbulence in a laboratory surf zone. *Coastal Engineering*, 24(1–2), 51–80.
- Ting, F. C. K., & Kirby, J. T. (1995). Dynamics of surf-zone turbulence in a strong plunging breaker. *Coastal Engineering*, 24(3–4), 177–204.
- Ting, F. C. K., & Kirby, J. T. (1996). Dynamics of surf-zone turbulence in a spilling breaker. *Coastal Engineering*, 27(3–4), 131–160.
- van der A, D. A., O'Donoghue, T., Davies, A. G., & Ribberink, J. S. (2008). Effects of acceleration skewness on rough bed oscillatory boundary layer flow. In *Proceedings of the 31st International Conference on Coastal Engineering* (pp. 1583–1595). World Sci., Singapore.
- van der A, D. A., O'Donoghue, T., & Ribberink, J. S. (2009). Sheet flow sand transport processes in oscillatory flows with acceleration skewness Paper 133. In *Proc. Coastal Dynamics '09*. World Sci., Singapore.

- van der A, D. A., O'Donoghue, T., & Ribberink, J. S. (2010). Measurements of sheet flow transport in acceleration-skewed oscillatory flow and comparison with practical formulations. *Coastal Engineering*, 57(3), 331–342. <https://doi.org/10.1016/j.coastaleng.2009.11.006>
- Van Der Werf, J. J., Doucette, J. S., O'Donoghue, T., & Ribberink, J. S. (2007). Detailed measurements of velocities and suspended sand concentrations over full-scale ripples in regular oscillatory flow. *Journal of Geophysical Research*, 112, F02012. <https://doi.org/10.1029/2006JF000614>
- van der Zanden, J., van der A, D. A., Hurther, D., Cáceres, I., O'Donoghue, T., & Ribberink, J. (2016). Near-bed hydrodynamics and turbulence below a large-scale plunging breaking wave over a mobile barred bed profile. *Journal of Geophysical Research: Oceans*, 121, 6482–6506. <https://doi.org/10.1002/2016JC011909>
- van der Zanden, J., van der A, D. A., Hurther, D., Cáceres, I., O'Donoghue, T., Ribberink, J. (2017). Suspended sediment transport around a large-scale laboratory breaker bar. *Coastal Engineering*, 125, 51–69. <https://doi.org/10.1016/j.coastaleng.2017.03.007>
- van Rijn, L. C. (2007). Unified view of sediment transport by currents and waves II: Suspended transport. *Journal of Hydraulic Engineering*, 133(6), 668–689. [https://doi.org/10.1061/\(ASCE\)0733-9429\(2007\)133:6\(668\)](https://doi.org/10.1061/(ASCE)0733-9429(2007)133:6(668))
- van Thiel de Vries, J. S. M., Van Gent, M. R. A., Walstra, D. J. R., & Reniers, A. J. H. M. (2008). Analysis of dune erosion processes in large-scale flume experiments. *Coastal Engineering*, 55(12), 1028–1040. <https://doi.org/10.1016/j.coastaleng.2008.04.004>
- Voulgaris, G., & Collins, M. B. (2000). Sediment resuspension on beaches: Response to breaking waves. *Marine Geology*, 167(1–2), 167–187.
- Walstra, D., Ruessink, B., Reniers, A., & Ranasinghe, R. (2015). Process-based modeling of kilometer-scale alongshore sandbar variability. *Earth Surface Processes and Landforms*, 40(8), 995–1005. <https://doi.org/10.1002/esp.3676>
- Watanabe, A., & Sato, S. (2004). A sheet-flow transport rate formula for asymmetric, forward-leaning waves and currents. In *Proceedings of the 29th International Conference on Coastal Engineering* (pp. 1703–1714). Lisbon, Portugal.
- Yoon, H.-D., & Cox, D. T. (2012). Cross-shore variation of intermittent sediment suspension and turbulence induced by depth-limited wave breaking. *Continental Shelf Research*, 47, 93–106. <https://doi.org/10.1016/j.csr.2012.07.001>